Supporting Information

Étienne et al. 10.1073/pnas.1417113112

SI Text

S1. Role of Microtubules. It has been reported that, in addition to the substrate, part (of the order of 13%) of the cortical tension could be balanced by the resistance to compression of microtubules (1). We have, thus, controlled the influence of microtubules in our setup, in particular for low external stiffness, which corresponds to lower length of cells and thus, is geometrically more likely to involve microtubule compression. The results, shown in Fig. S6, indicate that there is no such influence within experimental error. Thus, we neglect the role of microtubules compared with actomyosin tension and microplate resistance to bending in the modeling that follows.

S2. Model Derivation. As stated in the text, we are looking for the simplest model consistent with a dominant loss modulus at low frequencies in cell-scale rheological probing (2) and in vitro studies (3) and with the fact that cross-linkers in vivo are transient with a short residence time (4). Basic models of transiently cross-linked networks based on rubber-like models were first explored by Green and Tobolsky (5) and Yamamoto (6), and their nonlinear properties are still being investigated (7). Their response, up to the first order, turns out to be the same as the one of polymer solutions (that is, their stress–strain relationship is governed by Maxwell constitutive equation 1),

$$\tau_\alpha \overset{\triangledown}{\boldsymbol{\sigma}} + \boldsymbol{\sigma} - 2\tau_\alpha E \dot{\boldsymbol{\varepsilon}} = 0,$$

with $\boldsymbol{\sigma} = 2E(\beta^2 \langle \boldsymbol{RR} \rangle - \boldsymbol{I})$ (ref. 8, p. 116). The parameter $1/\beta$ corresponds to the reference length of the strand $\boldsymbol{R}$ in a state free of network stress. This reference length is set by thermal fluctuations, because networks of semiflexible actin filaments were shown to exhibit entropic elasticity (9). Here, the upper convected Maxwell tensor derivative $\overset{\triangledown}{\boldsymbol{\sigma}} = \dot{\boldsymbol{\sigma}} - \nabla \boldsymbol{v}^{\mathrm{T}} \boldsymbol{\sigma} - \boldsymbol{\sigma} \nabla \boldsymbol{v}$ takes into account the affine stretching of the strand vectors $\boldsymbol{R}$, the basic units of the network, by the velocity gradient $\nabla \boldsymbol{v}$. The difference is that, for polymer solutions, the time τ_α is the ratio of solvent viscosity to polymer elasticity, because this time is the characteristic time at which the polymers can deform relative to an affine global deformation of their surroundings (the solvent) (ref. 8, p. 116), whereas in the case of transiently cross-linked networks, τ_α is the characteristic unbinding time of the cross-links. Thus, the product $\tau_\alpha E$, which has the dimension of a viscosity, is only some apparent viscosity at the macroscopic scale and corresponds, in fact, to an elastic energy dissipation at rate $1/\tau_\alpha$. If there is a large number of cross-linkers present along a single filament, there will not be a single relaxation time τ_α but several (10). In this work, we choose to investigate the properties of the single relaxation time model above, which allows us to calculate analytically the model solution while retaining the essence of a long-time viscous-like and short-time elastic-like material.

A fraction α_{myo} of the cross-linkers considered is myosin bipolar filaments. In addition to their cross-linking role, they may effectuate a power stroke at a frequency $1/\tau_{\mathrm{myo}}$, which results in sliding the corresponding cross-linker by the myosin step length ℓ. If $\psi(\boldsymbol{\rho})$ is the orientational distribution function (8), power strokes appear as additional sink and source terms on the right-hand side of the probability balance equation,

$$\frac{\partial \psi}{\partial t} + \nabla_{\boldsymbol{\rho}} \cdot \left(\dot{\boldsymbol{R}} \psi \right) = \frac{\alpha_{\mathrm{myo}}}{\tau_{\mathrm{myo}}} \left(-\psi(\boldsymbol{\rho}) + \frac{1}{2}\psi(\boldsymbol{\rho} - \ell\boldsymbol{\rho}/|\boldsymbol{\rho}|) + \frac{1}{2}\psi(\boldsymbol{\rho} + \ell\boldsymbol{\rho}/|\boldsymbol{\rho}|) \right) \simeq \frac{\alpha_{\mathrm{myo}} \ell^2}{2\tau_{\mathrm{myo}}} \frac{\partial^2 \psi}{\partial |\boldsymbol{\rho}|^2}, \qquad \textbf{[S1]}$$

which multiplied by $\boldsymbol{\rho}\boldsymbol{\rho}$ and integrated over all configurations, yields an additional term of contractility:

$$\tau_\alpha \overset{\triangledown}{\boldsymbol{\sigma}} + \boldsymbol{\sigma} - 2\tau_\alpha E \dot{\boldsymbol{\varepsilon}} = \boldsymbol{\sigma}_{\mathrm{a}} = \sigma_{\mathrm{a}} \boldsymbol{A},$$

where $\sigma_{\mathrm{a}} = E\tau_\alpha / \tau_{\mathrm{myo}} \alpha_{\mathrm{myo}} (\ell\beta)^2$ is proportional to the myosin concentration and power stroke frequency. The tensor $\boldsymbol{A}$ is the local orientation tensor of the actin fibers:

$$\boldsymbol{A} = \int_{\boldsymbol{\rho}} \frac{\boldsymbol{\rho}\boldsymbol{\rho}}{|\boldsymbol{\rho}|^2} \psi \, \mathrm{d}\boldsymbol{\rho}.$$

The ratio of the apparent viscosity $\tau_\alpha E$ and contractile stress σ_{a} provides us with another characteristic time, $\tau_{\mathrm{c}} = 2\tau_\alpha E / \sigma_{\mathrm{a}} = 2\tau_{\mathrm{myo}} \alpha_{\mathrm{myo}}^{-1} (\ell\beta)^{-2}$, which characterizes the dynamics of shrinking of an actomyosin network in the absence of cross-linkers, which is the case in experiments in vitro (3).

Note that both characteristic times of cross-linker unbinding τ_α and myosin power stroke τ_{myo} have been taken as constants independent of the stress or strain to which they are submitted. It is, of course, well-established that there is a dependence of these parameters on stress and strain (11–13), which introduces nonlinearities in the model. An important unsolved question is to determine whether these dependences are or are not major players in the cell-scale mechanical behavior of actomyosin (e.g., through a stress-driven ripping of cross-links). Because their effect is a nonlinear variation of the above model, we study the linear response first (with constant characteristics times) before considering the full nonlinear model in *SI Text*, *S3.9*. It is found that the linear model is sufficient to reproduce the experimental data (that is, for our experiments, collective effects explain the observed behavior by themselves). Note that collective effects are also sufficient in Huxley's (14) model of muscle contraction, where Huxley (14) observes (ref. 14, p. 290) that assuming specific force-dependent binding kinetics only tunes the system's efficiency, not affecting its ability to fit Hill's force–velocity experimental observations.

The model obtained is the one of a viscoelastic liquid, in line with the seminal model by He and Dembo (15), who modeled the cytoskeleton as a viscous fluid and used it in numerical simulations of the cytokinesis. This modeling approach is also similar to the actin dynamics part of the model used by ref. 16 to simulate keratocyte migration. We provide above a microstructure-based derivation of this class of models, which allows us to interpret the dissipation in terms of molecular behaviors (discussion on Hill's law in *SI Text*, *S3.5*). This type of model, to the best of our knowledge, was never used to study mechanosensing behaviors of single cells. In the sequel (*SI Text*, *S4.2*), we compare it to models that have been used to analyze cell-scale mechanosensing but will first investigate its basic predictions.

S3. 1D Problem.

S3.1. In the absence of treadmilling. In this section, we investigate the behavior of a material modeled by the constitutive law (Eq. **2**) in a simplified, 1D geometry described in Fig. 3*B*. The actomyosin network is assumed to occupy an infinite cuboid between two horizontal plates: one of which is fixed, and the vertical position of the other is governed by a spring of stiffness k/S (per unit area) and equilibrium distance with the other plate L_0. If the current distance between the plates is L, the force exerted by the top plate on the material is, thus, $F/S = k(L_0 - L)/S$ per unit area.

We assume that the bulk forces acting on the actomyosin network (such as the friction with the cytosol) are negligible compared with the force developed by myosin contraction, thus

$$\nabla \cdot \boldsymbol{\sigma} = 0, \qquad \textbf{[S2]}$$

with the boundary condition $\boldsymbol{\sigma} \boldsymbol{e}_z = (F/S)\, \boldsymbol{e}_z$ at the upper plate, and corresponds to neglecting friction with the cytosolic fluid in the balance between the actomyosin stress and the force at the plates. By symmetry, only the vertical component σ_{zz} of the stress tensor $\boldsymbol{\sigma}$ in the actomyosin material is nonzero. We denote it ζ; from the above, we have $\partial_z \zeta = 0$, and thus, the boundary condition imposes $\zeta = F/S = k(L_0 - L)/S$ at every z. The stress is fully transmitted through the material. However, the rate-of-strain tensor $\dot{\boldsymbol{\varepsilon}}$ is also limited to a vertical component $\dot{\varepsilon} = \dot{L}/L$. Using these equalities, the constitutive Eq. **2** describes the complete dynamics of the system.

The mechanical response of this 1D case can be schematized by a spring-and-dashpot system as in Fig. S5*C* by noticing that we can decompose the strain rate as

$$\dot{\varepsilon} = \dot{\varepsilon}_1 + \dot{\varepsilon}_2 + \dot{\varepsilon}_3 = -\frac{\sigma_a}{2\tau_a E} + \frac{\zeta}{2\tau_a E} + \frac{\overset{\triangledown}{\zeta}}{E}.$$

The second and third terms are classical viscous and elastic rates of strain that can be represented as a spring and a dashpot, respectively. The first one is not classical and may be represented as a winding reel of constant rate of strain $\dot{\varepsilon}_1 = -\sigma_a/2\tau_a E$. Alternatively, we choose to represent it as a generator of constant tension $2\sigma_a$ in parallel with a dashpot of viscosity $4\tau_a E$, in order to illustrate better the dissipation that occurs when myosin is working, which will appear below. (When a dashpot of viscosity η is in parallel with a generator of constant tension $2\sigma_a$, the rate of strain is $\dot{\varepsilon}_1 = \zeta_{\text{dashpot}}/\eta$, where ζ_{dashpot} is the stress in the dashpot, such that the total stress is $\zeta = \zeta_{\text{dashpot}} + 2\sigma_a$. Hence, $\dot{\varepsilon}_1 = (\zeta - 2\sigma_a)/\eta$.) For this choice, one obtains that the different elements need to behave as

$$\dot{\varepsilon}_1 = \frac{\zeta - 2\sigma_a}{4\tau_a E} \quad \text{Generator of tension in parallel with a dashpot,}$$
$$\dot{\varepsilon}_2 = \frac{\zeta}{4\tau_a E} \quad \text{dashpot, and}$$
$$\varepsilon_3 = \frac{\zeta}{2E} \quad \text{spring.}$$

With this rheology, a permanent regime ($\dot{\varepsilon} = 0$ and $\dot{\zeta} = 0$) is reached for

$$F_p = \zeta_p S = \frac{\sigma_a S}{2}\left(\frac{k + k_c}{k_c} - \sqrt{\left(\frac{k + k_c}{k_c}\right)^2 - \frac{4k}{k_c}}\right) = \begin{cases} kL_0 & \text{if } k < k_c, \\ \sigma_a S & \text{else} \end{cases} \qquad \textbf{[S3]}$$

with $k_c = \sigma_a S/L_0$. The actomyosin model's response is, thus, very close to the behavior of a spring of stiffness k_c and free length = 0 when put in series with an external spring of stiffness k. Indeed, the asymptotes are the same for $k \to 0$ and $k \to \infty$ (Fig. 3*C*), which is not obvious, because in the permanent regime, the model only includes viscous dissipation and contractility. We have, thus, shown that a contractile fluid behaves like a spring in these conditions.

Indeed, when the cell is pulling on a spring of stiffness k, the maximum deflection that it can impose to the spring is L_0 (e.g., the initial cell length and consequently, the maximum length that it can shorten). However, this maximum deflection is achieved only if the maximum force generated by the cell $\sigma_a S$ is larger than the external spring force at maximum deflection kL_0; in other words, only if k is lower than $k_c = \sigma_a S/L_0$. In that case, the force reached is kL_0 and thus, proportional to k. In the other case ($k > k_c$), the deflection is less than L_0 and set by having an equal tension $\sigma_a S$ in both the external equivalent spring k and the cell.

One can get some mechanistic understanding of why the collective behavior of actomyosin as modeled in Eq. **2** gives this result using the schematic of the equation in Fig. S5*C*, although it is important to bear in mind that the schematics are not representing the actual mechanical processes at molecular scale but only provide a system that can be modeled with the same equation as Eq. **2**.

In the case of infinite external stiffness k, it is impossible to deflect the plates, and thus, $\varepsilon = 0$. After a transient state, a steady state is attained, with F and, thus, ζ reaching a plateau value (which we have to determine). Thus, the spring element also reaches a plateau elongation $\varepsilon_3 = \zeta/(2E)$. Hence, because $\dot{\varepsilon}_1 + \dot{\varepsilon}_2 + \dot{\varepsilon}_3 = 0$, we have

$$\dot{\varepsilon}_2 = -\dot{\varepsilon}_1 = \frac{\zeta}{4\tau_\alpha E} = -\frac{2\sigma_a - \zeta}{4\tau_\alpha E},$$

and from that, $\zeta = \sigma_a$. The two nonzero strains $\dot{\varepsilon}_1 = -\dot{\varepsilon}_2$ compensate internally and dissipate away the energy provided by myosin motors through the term σ_a.

In the other extreme of $k = 0$, the tension ζ is zero in the spring ($\varepsilon_3 = 0$) and dashpot ($\dot{\varepsilon}_2 = 0$). Hence, the tension in the other dashpot is $-2\sigma_a$, which as a result, will contract at a rate of $\dot{\varepsilon}_1 = -\sigma_a/(2\tau_\alpha E) = -1/\tau_c$. This contraction illustrates the dissipation of myosin energy internally by a viscous-like effect, causing a sustained deflection of the microplate until some equilibrium length is reached, which is explained in the following section.

S3.2. In the presence of treadmilling. We now introduce the fact that actin filaments in vivo are constantly being polymerized from one end (plus end) and depolymerized, mostly from the other (minus end), which results in the so-called treadmilling phenomenon (17). Assuming that this treadmilling is at steady state in the cell on average at the relevant timescale of our experiment, the effect of treadmilling in the bulk does not affect the modeling assumptions done in *SI Text*, *S2*: the elastic modulus E of the cross-linked network at any instant will have a constant average. However, at the boundary, some filaments will have their plus end oriented toward the boundary, and thus, polymerization of these will entail a net extension of the material (before stress equilibration depending on the boundary conditions).

In the framework of our 1D toy problem, this extension introduces a drift between the deformation of the material and the displacement of the boundary, which can be expressed as

$$\dot{L} = L\dot{\varepsilon} + 2v_t, \qquad \textbf{[S4]}$$

with v_t as the treadmilling speed (that is, the speed at which actin protrudes at the edge) (Fig. 3*D*). The factor 2 is caused by this effect taking place at both ends of our 1D sample.

When injected into the constitutive model, Eq. **S4** modifies the level of force (and length L_p) in the permanent regime:

$$F_p = \zeta_p S = \frac{\sigma_a S}{2}\left(\frac{k+k_c}{k_c} - \sqrt{\left(\frac{k+k_c}{k_c}\right)^2 - \frac{4k}{\sigma_a S}(L_0 - L_e)}\right), \qquad \textbf{[S5]}$$

with a modified critical stiffness $k_c = \sigma_a S/(L_0 + L_\alpha)$. Here, $L_\alpha = 4\tau_\alpha v_t$ is a characteristic elastic length of newly polymerized material. The critical stiffness k_c is lowered in proportion with the corresponding relative increase of height. We have also introduced another parameter, the length $L_e = 2\tau_c v_t = 4\tau_{myo} v_t/[(\ell\beta)^2 \alpha_{myo}]$. This length is discussed in the text; it is a tradeoff between the rate at which actin contracts under the effect of myosin and the speed at which the actin network expands by polymerization at its edges. It defines the shortest length that the cell achieves in the 1D model, when the stiffness of the plates is vanishingly small: in that case, all of the work of myosins is spent in contracting the part of the actin network newly polymerized.

For a low stiffness, this expression has for asymptote $F_p \sim k(L_0 - L_e)$, and for a large stiffness,

$$F_p \to \sigma_a S \frac{L_0 - L_e}{L_0 + L_\alpha}. \qquad \textbf{[S6]}$$

Treadmilling does not change the qualitative spring-like response of the material, but the equilibrium length of the equivalent spring is not zero anymore but L_e. As the device stiffness goes to zero, the length of the model meshwork will tend to $L_e = 2\tau_c v_t$, which is a dynamic balance between the speed $2v_t$ at which new material is added at the two boundaries (modeling polymerization) and the rate $1/\tau_c$ at which the existing material is contracted by the myosin motors. Inside this model material, even after the final length L_e is reached and the boundaries are immobile, there remains a continuous centripetal flow (Fig. 1*C*) that is very reminiscent of the retrograde actin flow observed in both crawling (17) and immobile spread cells (18). Exactly as in these cases, retrograde flow is made possible by depolymerization inside the model material. This behavior induced by treadmilling is an additional source of energy dissipation in the steady state, when the cell is apparently at equilibrium with constant length L_e and force F_p.

S3.3. Dynamics. The above constitutive and force balance equations can be written in terms of one equation only with the tension as the unknown:

$$\frac{\partial \zeta}{\partial t} = \frac{\sigma_a(k(L_0 - L_e)/S - \zeta) + \zeta(\zeta - k(L_0 + L_\alpha))}{\tau_c \sigma_a + \tau_\alpha(\zeta + kL_0/S)}. \qquad \textbf{[S7]}$$

One can analyze the rate of tension increase when the system begins to pull and ζ is still much smaller than σ_a for a low stiffness $k \ll ES/L_0$:

$$\frac{\partial F}{\partial t} = \frac{k(L_0 - L_e) - F(t)}{\tau_c} \sim \frac{F_p(k) - F(t)}{\tau_c}. \qquad \textbf{[S8]}$$

Also, for high stiffness, $k \gg ES/L_0$:

$$\frac{\partial F}{\partial t}=\frac{\sigma_a S(L_0-L_e)-F(t)(L_0+L_\alpha)}{\tau_\alpha L_0}=\frac{\left(F_p(k)-F(t)\right)(L_0+L_\alpha)}{\tau_\alpha\, L_0}. \quad \textbf{[S9]}$$

Experiments for very low values of the microplate stiffness k allow us to identify the parameters τ_c and v_t of the model.

From $n=9$ experiments with $k\leq 1.6$ nN/μm, we find $2\tau_c v_t = L_e = 6.6\pm 1.1$μm and $L_0 = 13.2\pm 0.1$μm. These values are consistent with the fact that $\partial F/(\partial k)=L_0-L_e=6.8\pm 0.4$μm in ref. 19. Additionally, the maximum force attained F_p, the current force $F(t)$, and the rate of growth of this force $\partial F/\partial t$ allow us to calculate τ_c using Eq. **S8**: $\tau_c=(F_p-F(t))(\partial F/\partial t)^{-1}=521\pm 57$ s. This value yields $v_t=6.5\pm 1.5$ nm/s, which is consistent with the literature (18) as stated in the text.

S3.4. Response to a step change of external stiffness. In ref. 20, we are able to vary instantaneously (within 0.1 s) the stiffness k of the external spring while ensuring that there is no instantaneous change of the force F felt by the cell or the microplate spacing L. In the modeling, these experimental conditions correspond to an instantaneous change of both k and L_0 at time t^*, such that F and L are continuous. We can, thus, write the following relations ensured by the experimental setup:

$$k(t)=\begin{cases} k_0, & t<t^*, \\ k_1, & t>t^*, \end{cases}$$

$$F(t)=F^*+\phi(t), \quad L(t)=L^*-\frac{\phi(t)}{k(t)},$$

where $\phi(t)$ is the variation of force around the force at time t^* [$\phi(t^*)=0$].

Changing only the stiffness in this manner ensures that the cell does not feel any step change: indeed, force and geometry are preserved, and the only change is the response of the microdevice to a variation of the force applied to it. The experimental result is that, despite the fact that none of the physical observables have been changed for the cell, its rate of loading $\partial F/\partial t$ of the device is instantaneously modified. In ref. 20, it is found that, when going from a stiffness k_0 to a stiffness k_1, the new rate of loading matches the rate of loading that the same cell type exhibits in a constant stiffness $k=k_1$ experiment at a time such that $F=F^*$. In ref. 21, this experiment is repeated with another cell type, and it is also found that the rate of loading is instantaneously changed. However, the value $\partial F/\partial t$ for $t\gtrsim t^*$ exhibits an overshoot: it is initially different from the value of the corresponding constant stiffness experiment and exhibits a relaxation toward it.

We can rewrite Eq. **S7** around $\zeta^*=F^*/S$, and we find

$$\frac{\partial F}{\partial t}(t^*)=k(t)\frac{L^*(\sigma_a S-F^*)-L_\alpha F^*-L_e\sigma_a S}{\tau_c\sigma_a S+\tau_\alpha(k(t)L^*+2F^*)}. \quad \textbf{[S10]}$$

The result is, thus, a step function, with a value for $t\gtrsim t^*$ that is exactly the rate of growth predicted by the model for a constant stiffness experiment with $k=k_1$. This model prediction corresponds to the experimental results in both refs. 20 and 21, except for the overshoot found in the latter.

The step change of the rate of loading can, thus, be explained by a purely intrinsic property of the cell's cytoskeleton as developed in the text.

In ref. 21, a model is proposed that accounts for a step change and relaxation as they are observed experimentally. However, this model has limited validity around t^* and breaks down at long times, predicting infinite force. Here, our model originally aiming at describing the long-time behavior of the cell depending on stiffness predicts the main feature of the experiments (the step change of the rate of loading) but not the overshoot found in one of the experiments. Our model, however, may produce this type of overshoot if more than a single relaxation time is used. This refinement of the model would correspond to replacing the spring k_1 in the model in ref. 21 by our viscoelastic constitutive equation. We find that such a refinement is not necessary to explain the data studied here.

In Fig. 2*C*, we give a numerical simulation result that corroborates the step change of $\partial F/\partial t$ found in Eq. **S10** and can be compared with an experimental curve without any parameter adjustment. The time profile of the microplate effective stiffness is imposed to be the same in the numerical simulation as in the experiment. The profile of force increase obtained presents the same instantaneous change of slope as the stiffness is varied, and the overall profiles match quantitatively.

S3.5. Hill's law. We examine the power dissipation predicted by the 1D model between two boundaries. The boundaries move toward the sample at velocity v (which is, thus, positive when the sample contracts) and feel a force F exerted by the sample (positive in the direction of contraction).

Hill's historical experiment (22) takes place at a constant level of force F. Our experiments (19), however, prescribe a relationship between F and v through the microplate stiffness $\partial F/\partial t=-kv$. Both can scan the F–v relationship by varying F for the former or k for the latter (in the case of ref. 19, we needed to investigate this relationship for a fixed $L=L_0-\delta$, where δ is small) (Fig. 4*A* and Fig. S5*A*). The calculation below does not require us to use either of these experimental ways to scan the F–v relationship. It relies only on the material properties of the sample.

As above, the mechanical equilibrium of the sample imposes that the vertical component of the stress tensor ζ is equal to F/S. Also, treadmilling produces a mismatch between the plate velocity $v=\dot{L}$ and the recoil of the existing network at the plate $-L\dot{\varepsilon}$ expressed by $v=-L\dot{\varepsilon}+2v_t$ (Eq. **S4**). These relations can be injected into the constitutive Eq. **2**:

$$\tau_\alpha\left(\dot{F}-2\dot{\varepsilon}F\right)+F-2\tau_\alpha ES\dot{\varepsilon}=\sigma_a S.$$

We recover a virtual work formulation by multiplying this by the velocity $L/(2\tau_\alpha)$. Adding the constant $ESL/(2\tau_\alpha)$ to both sides, this work can now be factorized in the manner of Hill's law:

$$\left(\frac{F}{S}+E\right)\left(v+2v_{\mathrm{t}}+\frac{L}{2\tau_\alpha}\right)=(\sigma_{\mathrm{a}}+E)\frac{L}{2\tau_\alpha}-\frac{L}{2S}\dot{F}. \qquad \textbf{[S11]}$$

The meaning of some of these terms is explained in the text.

In the case when the velocity v is zero, the force generated is finite as calculated above in Eq. **S6**, which can also write as

$$\frac{F_{\max}}{S}=\sigma_{\mathrm{a}}\left(1-\frac{E+\sigma_{\mathrm{a}}}{\sigma_{\mathrm{a}}}\frac{2v_{\mathrm{t}}}{v_\alpha+2v_{\mathrm{t}}}\right).$$

Even if both v and v_{t} are zero, and thus, the actomyosin does not contract macroscopically ($\dot{\varepsilon}=0$), the force generated remains finite, because it does work at a molecular scale. Actin polymerization, by adding new material at the edges, introduces a boundary creep, which consumes additional work in conditions of fixed length ($v=0$).

As stated in the text, apart from the polymerization boundary creep, the dissipative mechanism is the same as in the model of muscle contraction by Huxley (14). In this model, myosin elastic tails are prestretched preferentially in one direction before binding the actin thin filament. When there is no net sliding ($v=0$), they eventually unbind without having had the opportunity to provide work (that is, they have conserved this level of stretching). Although this fact is not explicitly written in the 1957 paper by Huxley (14), the prestretch that had been bestowed on the myosin elastic tail is, thus, lost.

The zero force $F=0$ condition is a (theoretical) limit corresponding to zero stiffness of the microplate. This limit is not attainable experimentally, because cells do not spread on both plates if their displacement does not generate any external force, which corresponds to the impossibility to apply any normal force to the plates. This effect probably has to do with the mechanism of force reinforcement of adhesions. In the model, however, the limit can be studied and yields a maximum velocity

$$v_{\max}+2v_{\mathrm{t}}=\frac{\sigma_{\mathrm{a}}v_\alpha}{E}=\frac{L}{\tau_{\mathrm{c}}}.$$

This velocity corresponds to the power injected by the myosin motors divided by the elastic modulus of the cross-linked network (minus the treadmilling contribution): indeed, in this limit, the myosins work against the elasticity of the actomyosin itself. The maximum velocity is, thus, limited by the rate τ_α at which the actin network fluidizes thanks to the detachment of cross-linkers. Compared with the case of muscles, actin treadmilling reduces the maximum speed of shortening by $2v_{\mathrm{t}}$, because the receding speed of the edge of the actin network must compensate for this speed of protrusion. Quantitatively, using the values obtained in *SI Text*, *S3.3*, we predict $v_{\max}\simeq 12.3$ nm/s, which is very close to $v_{\max}=13$ nm/s published in ref. 19.

Again, the dissipation here is of the same nature as for muscles in the model by Huxley (14): in his case, the only cross-linkers between thin and thick filaments are myosin heads, and zero force is obtained at the finite velocity at which the work rate performed by pulling myosin heads is exactly balanced by the work rate needed to deform myosin heads that have not yet detached from the actin filament. They will eventually detach, thus dissipating at a fixed rate the elastic energy that has been transferred to them.

When neither F nor v is zero, there is nonzero productive work performed on the plates. Because of the existence of maximum force and velocity, it is necessarily written

$$\frac{Fv}{F_{\max}v_{\max}}=r\left(1-\frac{F}{F_{\max}}-\frac{v}{v_{\max}}\right).$$

In both the experiments by Hill (22) and our experiments (19), r is found to be mostly independent of F and v, and $r\simeq 0.25$. In Huxley's model of muscles, r is a signature of the preferential prestretch of myosins that models the power stroke normalized by the detachment rate (14, 23). In our model of cells, $2r\simeq\tau_c/\tau_\alpha$ is the ratio of the characteristic times of contraction and stress relaxation through cross-linker unbinding. This observation does not explain the coincidence of finding the same value of r in both cells and muscles; however, we note that this parameter has a similar signification in both models.

Specifically,

$$r=\frac{E}{\sigma_{\mathrm{a}}\left(1-\frac{E+\sigma_{\mathrm{a}}}{\sigma_{\mathrm{a}}}\frac{2v_{\mathrm{t}}}{v_\alpha+2v_{\mathrm{t}}}\right)}. \qquad \textbf{[S12]}$$

Thus, in our case, Hill's parameter r is such that

$$\frac{E}{\sigma_{\mathrm{a}}}=\frac{\tau_c}{2\tau_\alpha}\le r\le\frac{\tau_c}{2\tau_\alpha}+\left(\frac{\tau_c}{2\tau_\alpha}\right)^2, \qquad \textbf{[S13]}$$

depending on v_{t}.

Note that these equations can be applied to the actomyosin pushing against an obstacle, with $0\le -F\le ES$ and $0\le -v\le v_{\mathrm{t}}$.

S3.6. Quantitative analysis. Because $r\simeq 0.25$ in experiments (19), τ_c/τ_α has to be in the range 0.4–0.5; thus, because $\tau_c=521\pm 57$ s, we have $\tau_\alpha=1,186\pm 258$ s. In turn, using also $v_{\mathrm{t}}=6.5$ nm/s (*SI Text*, *S3.3*), we find $\sigma_{\mathrm{a}}S=F_{\max}(L_0+L_\alpha)/(L_0-L_e)=(2.0\pm\ 0.9)\cdot 10^3$ nN ($n=13$). Thus, the four parameters of the 1D model, namely τ_α, τ_c, v_{t}, and $\sigma_{\mathrm{a}}S$, are identified using only the average maximum force (equilibrium of infinite stiffness experiments), maximum velocity (dynamics of experiments with very low stiffness), and shortest length at equilibrium (experiments with very low stiffness) plus the shape of the Hill-type law (parameter r).

The other experimental data (stiffness dependence of the force [Fig. 3*C*], dynamics as the microplate stiffness is modified [Fig. 2*C*], and values of $F(t)$ at $L_0 - L = 1\mu$m [Fig. 4*A*]) are matched by the model without any adjustable parameter [e.g., the values found yield a critical stiffness $k_c = \sigma_a S/(L_0 + 4\tau_\alpha v_t) = 41$ nN/μm, which is consistent with the experimental results] (Fig. 3*C*).

Moreover, the values for τ_c, τ_α, and especially, v_t are independently measurable and consistent with the literature (in the text).

S3.7. Blebbistatin experiments. We check that the model predicts correctly the decrease of the plateau force that is recorded in experiments with infinite microplate stiffness when an increasing dose of blebbistatin is used to prevent myosin activity (19). We expect that the fraction α_{myo} will decrease according to the inhibition of myosin-II ATPase activity:

$$\alpha_{myo}^{[Blebb]} = \alpha_{myo} \frac{K_i}{K_i + [Blebb]},$$

where K_i is the inhibitory constant. Because σ_a is proportional to $\alpha_{myo}^{[Blebb]}$ and following Eq. **S5**, the predicted plateau force will decrease with $\alpha_{myo}^{[Blebb]}$. This prediction coincides with what is observed experimentally (19) and reported in Fig. 2*D*, *Inset*, where the prediction of the decrease of plateau force is shown to match closely the one observed experimentally. The inhibitory constant K_i used in Fig. 2*D* is $K_i = 2.8$ μM, similar to that measured experimentally in mouse cardiac muscles (24).

When running the model with the modified fraction α_{myo}, we obtain the prediction of a shift in the mechanoresponse of cells: the maximum force exerted by cells is lower, as expected, and this saturating force is reached for a reduced critical stiffness $k_c^{[Blebb]} = k_c \alpha_{myo}^{[Blebb]}/\alpha_{myo}$. Below $k_c^{[Blebb]}$, the force exerted by cells for a given external stiffness is predicted to tend to the same trend as in control conditions. These model predictions match well with experimental results (Fig. 2*D*).

S3.8. Mechanical energy budget and metabolism. The experiments give access to the maximal mechanical power that the cell can develop (around 0.5 fW for some optimal load $F \simeq 120$ nN) (Fig. 4*B*). As discussed in *SI Text*, *S3.5*, this power goes to zero when the load is too high and the cell stalls ($F = F_{max}$) and of course, when the load is zero. The model explains this by describing the dissipative phenomena that are at play at a molecular scale in the cascade of events from myosin power strokes down to the mechanical action on microplates. Because these dissipative terms are expressed in terms of the same quantities as the effective mechanical work of the cell (namely the four parameters E, τ_α, σ_a, and v_t), we are able to evaluate the dissipated power through each of these mechanisms (Fig. 4*B*). The total of these dissipative terms and the mechanical power corresponds to the total mechanical power provided by myosin power strokes and is evaluated around 10 fW.

It is instructive to compare these 10 fW spent in mechanics with both what was actually transmitted to the cell's environment (0.5 fW at best) and the total power that is being injected in all of the cell's functions (that is, the metabolic rate, which is estimated around 30 pW for a single cell) (25). On the one hand, the mechanical efficiency of our nonmuscle cells seems to be rather low, because only 5% of the power provided by myosins is actually being used to act on the cell's environment. On the other hand, 10 fW of 30 pW is a very low share in the total energy budget of the cell. In the text, we argue that this relatively low energetic cost is a plausible reason why evolutionary pressure would not have led to an increase of efficiency in nonmuscle cells.

We can verify that this value of 10 fW is plausible with respect to what is known on the expenditure of metabolic energy in single cells: ATPase receives some 60% of the metabolic power (26) (thus, around 20 pW), 90% of which goes to protein synthesis, RNA/DNA synthesis, and calcium and sodium cycling. The remaining power, of the order of 10^3 fW, must be distributed between all mechanisms based on ATP-consuming molecular motors and also, actin turnover. Our estimate of 10 fW for the share of this going to myosin could, thus, plausibly be one order of magnitude too low. Because this figure is being obtained only from the modeling of the dynamics of contraction of cells in the microplate setup, it is an acceptable level of error.

S3.9. Nonlinear extensions of the model. The binding kinetics of actin cross-linkers have been shown to be dependent on the mechanical stress that is felt locally [e.g., α-actinin-4 is a catch bond with binding affinity that is higher when under load (12), a property characteristic of catch bond-like behavior]. Also, myosin molecules are known to stall when the tension is too high (13). Here, we investigate in what degree these molecular sensitivities to stress affect mechanical behavior that emerges out of their collective dynamics according to the predictions of this model.

Cross-linkers stress-dependent affinity. The first-order correction to the cross-linker bond lifetime τ_α is $\tau_\alpha = \tau_\alpha^0 + \tau_\alpha^1 \sigma/E$, where τ_α^0 is the zero stress average lifetime, and τ_α^1 is an additional lag positive for catch bonds and negative for slip bonds. Injected into Eq. **2** and following the same procedure as in *SI Text*, *S3.2*, we obtain the equation governing the plateau height H_p as a function of external stiffness k:

$$\frac{k}{S}(H_0 - H_p)\left(H_p + 4\left(\tau_\alpha^0 + \tau_\alpha^1 \frac{k}{ES}(H_0 - H_p)\right)v_t\right) = -2k\left(\tau_\alpha^0 + \tau_\alpha^1 \frac{k}{ES}(H_0 - H_p)\right)Ev_t + \sigma_a\left(1 + \frac{\tau_\alpha^1 k}{\tau_\alpha^0 ES}(H_0 - H_p)\right)H_p.$$

Solving for H_p, we obtain the behavior shown in Fig. S1*A*: in the catch bond case, the maximal force attained against stiff microplates is increased, whereas it is decreased in the slip bond case. For low stiffness, because the tension does not build up much in the actomyosin cortex, we have $\tau_\alpha \simeq \tau_\alpha^0$ and an unchanged behavior.

Myosin stalling. If we assume following ref. 27 that the rate at which myosin performs power strokes decreases with stress and take a linear law $1/\tau_{myo} = (1 - \lambda_{myo}\sigma/E)/\tau_{myo}^0$, the equation to be solved is

$$\frac{k}{S}(H_0 - H_p)(H_p + 4\tau_\alpha^0 v_t) = -2k\tau_\alpha^0 Ev_t + \sigma_a^0\left(1 - \lambda_{myo}\frac{k}{ES}(H_0 - H_p)\right)H_p,$$

where $\sigma_a^0 = E(\tau_\alpha/\tau_{myo}^0)\alpha_{myo}(\ell\beta)^2$. Results are shown in Fig. S1*B*. As above, at low external stiffness, the results do not change because stress does not build up much in the cortex. When external stiffness is high, myosin activity is reduced, and thus, the maximum force that can be attained is lower.

In sum, we obtain a shift of the maximum force exerted by cells against a stiff environment when catch bond cross-linker or stress-sensitive myosin dynamics are considered (Fig. S1). The shift is taking place in the expected direction: catch bonds lead to higher force, whereas slip bonds or stalling myosin lead to lower force. It is interesting to note that the overall profile of stiffness-dependent plateau force is not modified by these nonlinear variants of the rheological model. This robustness of the overall profile means that the collective effect that we describe using the linear model is rather robust with respect to the specific kinetics of the molecules. Another consequence is that, in the absence of direct measurement of these kinetics at the molecular scale during our cell-scale experiments, we cannot hope to determine from cell-scale behavior the modulation of the measured maximum force that is caused by these nonlinear effects.

S4. Comparison with Other Models of Rigidity-Dependent Response.

S4.1. Computational bottom-up models of actomyosin networks. Molecular dynamics of individual actin filaments and actin-binding proteins can be simulated numerically in a simple geometry (box) with boundary conditions that correspond to different stiffness of the surrounding. These simulations are an alternative to the analytical route chosen in *SI Text*, *S3.2* to test whether some rules of molecular interaction lead to rheologies that exhibit a differential response to external stiffness, although these computational approaches do not provide a rheological law such as Eq. **2**.

In ref. 28, Borau et al. consider molecular dynamics, including models of actin (no treadmilling), cross-linkers with affinity with actin that follow Bell's equation, and motors that have a Bell's affinity and stall against a predetermined force. They obtain a stiffness-dependent plateau stress, which has the same profile as in Fig. 3*C*, with $F_p \propto k$ against low stiffness and a constant F_p against high stiffness, but for reasons that are different: the maximum stress is set by the stall force of individual molecules (whereas it emerges from collective effects in our model).

When the external stiffness is low, the network contracts until a maximal strain is reached; this maximal strain corresponds to a jamming of motors along filaments (whereas the maximal strain in our model corresponds to a dynamic balance between myosin-driven contraction and polymerization-driven protrusion). These effects are also found by ref. 27, where the motors jam at the barbed end of filaments. In this case again, this network-scale stalling is caused by jamming of individual motor molecules in the models of refs. 27 and 28, whereas it emerges from the competition between network myosin-driven contraction and polymerization-driven growth in the case of our model (which is in agreement with the observations of actin retrograde flow in spreading cells).

These models, thus, offer alternative mechanisms by which stress and strain are limited during actomyosin contraction. These alternative mechanisms may combine with the collective effects that we describe, which are shown in *SI Text*, *S3.9*. Note that these alternative mechanisms do not predict a retrograde flow of actin after a plateau stress and strain are reached, whereas such a flow is observed in plated cells (18). It is likely that during cell contraction, these mechanisms and the collective effects that we describe appear combined to yield cell behavior. As noted in *SI Text*, *S3.9*, molecular-scale microscopy observing the dynamics of motors and cross-linkers during cell contraction would be necessary to determine the contribution of these nonlinear terms.

S4.2. Cell-scale phenomenological models. In refs. 29 and 30, the cell is modeled as a linear elastic body having an intrinsic equilibrium shape that is prestretched to some maximum strain. In our notation, their constitutive equation is

$$\boldsymbol{\sigma} = 2E(\boldsymbol{\varepsilon} - \boldsymbol{\varepsilon}_0),$$

with $\boldsymbol{\varepsilon}_0$ as an equilibrium shape that the cell would take in the absence of external stresses. This model is supplemented with a phenomenological feedback on the elastic modulus on the timescale of hours or days, which corresponds to the phenomenon of stress-fiber polarization (31). This long-term effect is out of the scope of our model and experiments; thus, our model compares with their model before this feedback comes into play. In a 1D setting, their model, thus, corresponds to the prestretched spring in Fig. 3*A*, which yields a stiffness dependence closely mimicking experimental data and our model predictions (Fig. 3*C*). Our model, in addition, provides a microstructure basis for this qualitative behavior and a quantitative reading of experiments; particularly, the equilibrium shape $\boldsymbol{\varepsilon}_0$ and cell stiffness k_c in ref. 29 are explicated as proportional to the product of a characteristic contraction time and the treadmilling speed, $\tau_c v_t$, and as the ratio of the myosin contractile stress and a length, $k_c = \sigma_a S/\ (L_0 + 4\tau_\alpha v_t)$, respectively.

In ref. 32, a model is introduced also in the framework of active gel theory. However, it resorts to the stress–strain relationship in ref. 29 so as to avoid calculating the orientation tensor Q_{ij} of the cytoskeleton and uses a 1D linear elastic stress–strain relationship; equation S7 in ref. 32 in our notation is $\sigma = 2E(L - L_e)$.

In ref. 33, a 1D viscoelastic solid model is presented; combining equations 2 and 5 in ref. 33 is in our notation

$$\sigma = 2E(L - L_e) + 2\eta\dot{L},$$

with $L_e = l_C^0 - F_S/k_C$ in their notation. Different from the previous models, the viscous term added in this model allows for the study of the dynamics of the cell shortening. However, the equilibrium shape in all three models is a static elastic balance between the environment resistance to deformation and a phenomenological internal elasticity, which corresponds to the spring model described in Fig. 3*A*.

S5. 3D Problem. In this section, we present a full 3D model of the cell mechanics as a contractile viscoelastic thin shell, obeying the rheological Eq. **2** and enclosing an incompressible cytosol. Forces are transmitted to the microplates at the contact line between the cell boundaries and the microplates.

S5.1. Geometry. It is seen from experimental observations that the cell boundaries connecting the plates are, in most cases, very well approximated by an arc of a circle (Fig. 1*C*). This shape had already been observed in the case of cells spread on a microneedle array having reached a stationary shape (34); in this setup, we find that it is also true while the cell is spreading (Fig. S3*A*).

When observing cells from the side, we assume that the cell shape is cylindrical. This assumption is supported by other experiments, where cells are observed from the bottom in TIRF (Fig. S3*B*). Thus, along the z-axis orthogonal to the microplates which have a location that is parameterized as $z = \pm l$, where l is the half-length of the cell, we can fit experimental results using the law

$$r(z) = R_c - \frac{1}{\kappa}\left(1 - \sqrt{1-(\kappa z)^2}\right), \qquad \textbf{[S14]}$$

where R_c is the radius at the cell equator ($z = 0$), and κ is the signed curvature in the vertical plane (Fig. 1*C*). The curvature κ evolves in time from a positive curvature ($t = 10$ s in Fig. S3*A*) to a negative one ($t = 120$ s and later in Fig. S3*A*).

To the physicist, it may be a surprise that the cell shape is not well-fitted by a surface of constant mean curvature, such as a catenoid. Indeed, although each boundary seen on Fig. S3*A* can be reasonably fitted with an hyperbolic cosine function, the asymptotes of these fits do not match: the cell shape is close to a minimal surface with a different weight on its curvatures, $\kappa\sigma + \kappa_\perp\sigma_\perp = 0$, where $\kappa_\perp$ is the curvature in a plane orthogonal to the side view. In light of Laplace law, these weights can be interpreted as tensions of different magnitude in the longitudinal ($\boldsymbol{e}_s$ in Fig. 1*C*) and orthoradial ($\boldsymbol{e}_\phi = \boldsymbol{e}_n \times \boldsymbol{e}_s$) directions. The reason for these different tensions and details of this Laplace law are given in the next section. We cannot fit the cell shape with an analytical function matching this law, because first, functions solving the corresponding differential equation have never been investigated and do not have the same properties as the hyperbolic cosine and second, the tensions σ and $\sigma_\perp$ actually vary in some measure along the vertical direction.

From this fitting, we can calculate the volume of the cell through time. Here again, the physicist is surprised to find that the volume defined by Eq. **S14** and the plate positions $z = \pm l$ are not a constant (Fig. S2). However, this volume is not the volume of the cell itself but the volume enclosed by the lateral cell boundaries: indeed, it is observed in side views of cells presenting such a large enclosed volume increase that the cell detaches from the microplates in the central region of the contact area (Fig. S2), forming a pocket between the cell membrane and the microplate, which has every reason to be filled by culture medium seeping between the adhesions seen in Fig. S3*B*. Although it was not possible to track the volume of these pockets through time and compare it with the enclosed volume variations, we can estimate the energetic cost of the corresponding water flow: adhesions are more than 1 μm apart over a 10- to 20-μm length between the periphery and the central region, where medium pocket is being formed. Assuming a low estimate of $N > 30$ passages of height 0.1 μm through which medium can flow from the periphery to the cell interior, we obtain that the pressure needed to drive the flow noted in Fig. S2 is about 10 Pa and that the power needed is of the order 10^{-17} W (that is, two orders of magnitude smaller than the actomyosin power transmitted to the microplate and measured in the experiments). The formation of such pockets is, thus, very plausible and indeed, observed in most experiments when the force is large.

The data that we present do not allow us to check whether the totality of the change of apparent volume is caused by this water seepage. Therefore, there may be also some volume variations because of a regulation of cell volume (35) superimposed to the one caused by the formation of the pocket. Although the accurate measurement of these variations would be important to understand the spreading dynamics of the cells in our setup, the model below does not require us to assume volume conservation to predict the vertical deflection dynamics of the microplates.

S5.2. State of stress of the actin cortex in experiments. Experiments of single-cell stretching (19) allow us to track simultaneously the geometry and force generated by cells between two microplates with an arbitrary stiffness (Fig. 1 and Figs. S2 and S3). To check whether the rheological model developed above can explain the observed cell behavior, we need to first calculate the state of stress within the actin cortex from the experimental observables.

Since it was shown in ref. 19 that the force generation in these experiments is caused by actomyosin contraction, we modeled the cells as an actomyosin surface (shell) surrounding an incompressible but passive cell body (cytosol, nucleus, and noncortical cytoskeleton), with mechanical action that is solely represented by a homogeneous internal pressure difference with the medium outside, $P = P_{\text{cell}} - P_{\text{medium}}$. Actomyosin being considered here as a thin structure, we perform the calculations in terms of a surface tension $w\boldsymbol{\sigma}$, where w is the thickness of the actomyosin cortex; $\boldsymbol{\sigma}$ is assumed to be a tensor tangential to the cortex and assumed to have no variation across w.

Because inertia is irrelevant at this scale, the spring force $F = 2k(l_0 - l)$ of the microplate device needs to be balanced at any instant by the combination of the cell body pressure force and the tension force in the cell cortex:

$$F = 2\pi R_p \; w\sigma|_{z=l} - \pi R_p^2 \, P. \qquad \textbf{[S15]}$$

Here, R_p is the radius of the cell at a microplate, and σ is the tension of the actomyosin cortex along the vertical direction. It is dependent on z and corresponds to the component σ along $\boldsymbol{e}_s\boldsymbol{e}_s$ of the stress tensor $\boldsymbol{\sigma}$ (Fig. 1*C*). Because of the symmetry and the assumption of a thin actomyosin cortex, this tensor can only have one other nonzero component along the orthoradial direction, $\sigma_\perp \boldsymbol{e}_\phi\boldsymbol{e}_\phi$. Using curvilinear coordinates, we can show that the force balance in the $\boldsymbol{e}_s$ and $\boldsymbol{e}_\phi$ directions at any position z writes

$$0 = P\boldsymbol{e}_n + \nabla\cdot\boldsymbol{\sigma} = \begin{pmatrix} P - \kappa w\sigma - \dfrac{\sin\theta}{r} w\sigma_\perp \\ w\dfrac{\partial\sigma}{\partial s} + \dfrac{\cos\theta}{r} w(\sigma - \sigma_\perp) \end{pmatrix}, \qquad \textbf{[S16]}$$

where the first line is Laplace law written with different tensions in the vertical and orthoradial directions, and the second line describes the equilibrium along direction $\boldsymbol{e}_s$.

To solve these equations, we need to specify the geometry of the actomyosin walls using Eq. **S14**. One can then use power series and get $\sigma = \sigma^0 + \sigma^1 z^2$ and $\sigma_\perp = \sigma_\perp^0 + \sigma_\perp^1 z^2$ in a closed form depending on geometrical parameters (l, R_c, and κ) and the pressure difference P:

$$\begin{aligned} \sigma &= \sigma^0 + z^2\frac{\kappa}{2}\left(\sigma^0\left(\frac{1}{R_c} + \kappa\right) - \frac{P}{w}\right) \\ \sigma_\perp &= R_c\left(P/w - \kappa\sigma^0\right) + z^2\kappa P/w\left(\kappa R_c - \frac{1}{2}\right) \end{aligned} \qquad \textbf{[S17]}$$

with

$$w\sigma^0 = \frac{1}{2}R_c P + \frac{F}{2\pi R_c}.$$

The presence of P in these equations means that we cannot read directly the state of stress of the actin cortex from its geometry and the measurement of F. However, if we have, for example, an indication on the orthoradial stress $\sigma_\perp$, which is possible when the shape is stationary and thus, no dissipation takes place in the orthoradial direction, then both P and σ can be determined. Note that, in this section, we have not made use of any assumption on the rheology of actomyosin; in particular, we have not used the constitutive Eq. **2** yet: the experimental observations fitted by a geometry are sufficient to describe the state of stress in the cortex.

S5.3. Equilibrium length and force. We apply the rheological model Eq. **2** to predict the rate of strain $\partial v_s/\partial s$ in the actin cortex along $\boldsymbol{e}_s$ and obtain its value as a power series in z and function of F_p, the geometry, and the model parameters τ_c, τ_α, and σ_a. Thus, we need to write the tensorial constitutive Eq. **2** in curvilinear coordinates, assuming that $\boldsymbol{A} = \boldsymbol{e}_s\boldsymbol{e}_s + \lambda \boldsymbol{e}_\phi \boldsymbol{e}_\phi$ (i.e., that the contractile stress in the orthoradial direction $\boldsymbol{e}_\phi$ is a fraction λ of the contractile stress orthogonal to the plates):

$$\begin{aligned}\tau_\alpha\left(\frac{\partial\sigma}{\partial t} + v_s\frac{\partial\sigma}{\partial s} - 2\left(\frac{\partial v_s}{\partial s} + \kappa v_n\right)\sigma\right) + \sigma - 2\tau_\alpha E\left(\frac{\partial v_s}{\partial s} + \kappa v_n\right) &= \sigma_a,\\ \tau_\alpha\left(\frac{\partial\sigma_\perp}{\partial t} - \frac{2}{r}(v_s\cos\theta + v_n\sin\theta)\sigma_\perp\right) + \sigma_\perp - \frac{2\tau_\alpha E}{r}(v_s\cos\theta + v_n\sin\theta) &= \lambda\sigma_a.\end{aligned} \quad \textbf{[S18]}$$

Let us consider a cell that has reached an equilibrium shape, such as the cell in Fig. S2, at time $t = 2{,}000$ s. The force plateaus at a value F_p, the curvature κ has reached a stable negative value, and the equator length $2\pi R_c$ is steady. Thus, $\dot{l} = 0$, $\dot{R}_c = 0$, $v_n = 0$, and the force does not evolve ($\dot{F} = 0$ and hence, $\partial\sigma/\partial t = 0$); these constitutive equations simplify to

$$\begin{aligned}\tau_\alpha v_s\frac{\partial\sigma}{\partial s} + \left(1 - 2\tau_\alpha\frac{\partial v_s}{\partial s}\right)\sigma - \tau_c\sigma_a\frac{\partial v_s}{\partial s} &= \sigma_a\\ \sigma_\perp &= \lambda\sigma_a.\end{aligned}$$

Using the force balance (Eq. **S17**), we can calculate $v_s(z)$ as a function of F_p:

$$v_s = z\left(-\frac{\phi}{\tau_c} + \frac{1-\phi}{2\tau_\alpha}\right)\left(1 + \frac{\kappa z^2}{6R_c}\left(\kappa R_c + \frac{2\tau_\alpha + \tau_c}{\tau_c}\phi\right)\right), \quad \textbf{[S19]}$$

where

$$\phi = \frac{2 - R_c\kappa}{2 - R_c\kappa + 2\dfrac{\tau_\alpha}{\tau_c}\left(\lambda + \dfrac{F_p}{\pi R_c\sigma_a}\right)} \in (0, 1].$$

This flow is the balance between a contractile term proportional to $1/\tau_c$ and an extensional term in $1/(2\tau_\alpha)$. In practice, it is always negative: it corresponds to a retrograde flow that vanishes at the cell's equator for obvious symmetry reasons and increases in magnitude with z. It is modulated by geometric factors but it is also modulated by the force F_p. This retrograde flow is present for all values of the external stiffness.

To reach an equilibrium, we need the retrograde flow to compensate exactly the addition of the new cortex through polymerization at $z = l$, which means that

$$v_s(l_p) = -v_t. \quad \textbf{[S20]}$$

Thus, we have a relation for l_p when the geometry is known in terms of R_c and κ. When the force F_p is low (in the case of vanishing k), there is an asymptote value l_e for l_p provided that it is much smaller than R_c, which is found to be the case. Experiments provide a redundant reading of l_e, because the force has to be $2k(l_0 - l_e)$ at low k values. Thus, we also have,

$$\lim_{k\to 0}\frac{\partial F_p}{\partial k} = 2(l_0 - l_e).$$

These redundant experimental observations consistently give $l_e/l_0 = 0.46 \pm 0.06$. In Eq. **S19**, l_e is proportional to $\tau_c v_t$ as in the 1D model but modulated by both the curvature (which is observed) and the contractility in the orthoradial direction, which cannot be accessed. Using the values $\tau_c = 521 \pm 57$ s and $\tau_\alpha = 1{,}186 \pm 258$ s obtained from the dynamics of the 1D model (*SI Text*, *S3.3*), it is found that the model can predict the cell behavior only if the orthoradial contractility $\sigma_{a,\perp} = \lambda\sigma_a$ is significantly lower than σ_a ($\lambda \lesssim 0.5$); otherwise, the pressure buildup in the cytosol prevents the cell from contracting. Thus, we take $\lambda = 0.5$ and $v_t = 4$ nm/s, which is close to the value found in 1D (6.5 ± 1.5 nm/s) and the literature (4.3 ± 1.2 nm/s) (18).

There remains one last free parameter in the 3D model, the (surfacic) contractility $w\sigma_a$. Its value can be assessed in the limit of infinite microplate stiffness k; we find $w\sigma_a = 15$ nN/μm. Using these values, the 3D model yields a plateau force very close to the one of the 1D model (Fig. 2*A*).

1. Stamenović D, Mijailovich SM, Tolić-Nørrelykke IM, Chen J, Wang N (2002) Cell prestress. II. Contribution of microtubules. *Am J Physiol Cell Physiol* 282(3):C617–C624.
2. Wottawah F, et al. (2005) Optical rheology of biological cells. *Phys Rev Lett* 94(9):098103.

3. Soares e Silva M, et al. (2011) Active multistage coarsening of actin networks driven by myosin motors. *Proc Natl Acad Sci USA* 108(23):9408–9413.
4. Fritzsche M, Lewalle A, Duke T, Kruse K, Charras G (2013) Analysis of turnover dynamics of the submembranous actin cortex. *Mol Biol Cell* 24(6):757–767.
5. Green MS, Tobolsky AV (1946) A new approach to the theory of relaxing polymeric media. *J Chem Phys* 14(2):80–92.
6. Yamamoto M (1956) The visco-elastic properties of network structure: I. General formalism. *J Phys Soc Jpn* 11(4):413–421.
7. Vaccaro A, Marrucci G (2000) A model for the nonlinear rheology of associating polymers. *J Nonnewt Fluid Mech* 92(2):261–273.
8. Larson RG (1999) *The Structure and Rheology of Complex Fluids*, Topics in Chemical Engineering (Oxford Univ Press, London).
9. Gardel ML, et al. (2004) Elastic behavior of cross-linked and bundled actin networks. *Science* 304(5675):1301–1305.
10. Broedersz CP, et al. (2010) Cross-link-governed dynamics of biopolymer networks. *Phys Rev Lett* 105(23):238101.
11. Kovács M, Thirumurugan K, Knight PJ, Sellers JR (2007) Load-dependent mechanism of nonmuscle myosin 2. *Proc Natl Acad Sci USA* 104(24):9994–9999.
12. Yao NY, et al. (2013) Stress-enhanced gelation: A dynamic nonlinearity of elasticity. *Phys Rev Lett* 110(1):018103.
13. Debold EP, Patlak JB, Warshaw DM (2005) Slip sliding away: Load-dependence of velocity generated by skeletal muscle myosin molecules in the laser trap. *Biophys J* 89(5):L34–L36.
14. Huxley AF (1957) Muscle structure and theories of contraction. *Prog Biophys Chem* 7:255–318.
15. He X, Dembo M (1997) On the mechanics of the first cleavage division of the sea urchin egg. *Exp Cell Res* 233(2):252–273.
16. Rubinstein B, Fournier MF, Jacobson K, Verkhovsky AB, Mogilner A (2009) Actin-myosin viscoelastic flow in the keratocyte lamellipod. *Biophys J* 97(7):1853–1863.
17. Mitchison TJ, Cramer LP (1996) Actin-based cell motility and cell locomotion. *Cell* 84(3):371–379.
18. Rossier OM, et al. (2010) Force generated by actomyosin contraction builds bridges between adhesive contacts. *EMBO J* 29(6):1055–1068.
19. Mitrossilis D, et al. (2009) Single-cell response to stiffness exhibits muscle-like behavior. *Proc Natl Acad Sci USA* 106(43):18243–18248.
20. Mitrossilis D, et al. (2010) Real-time single-cell response to stiffness. *Proc Natl Acad Sci USA* 107(38):16518–16523.
21. Crow A, et al. (2012) Contractile equilibration of single cells to step changes in extracellular stiffness. *Biophys J* 102(3):443–451.
22. Hill AV (1938) The heat of shortening and the dynamic constants of muscle. *Proc R Soc Lond B Biol Sci* 126(843):136–195.
23. Williams WO (2011) Huxley's model of muscle contraction with compliance. *J Elast* 105(1-2):365–380.
24. Dou Y, Arlock P, Arner A (2007) Blebbistatin specifically inhibits actin-myosin interaction in mouse cardiac muscle. *Am J Physiol Cell Physiol* 293(3):C1148–C1153.
25. West GB, Woodruff WH, Brown JH (2002) Allometric scaling of metabolic rate from molecules and mitochondria to cells and mammals. *Proc Natl Acad Sci USA* 99(Suppl 1): 2473–2478.
26. Buttgereit F, Brand MD (1995) A hierarchy of ATP-consuming processes in mammalian cells. *Biochem J* 312(Pt 1):163–167.
27. Parameswaran H, Lutchen KR, Suki B (2014) A computational model of the response of adherent cells to stretch and changes in substrate stiffness. *J Appl Physiol (1985)* 116(7): 825–834.
28. Borau C, Kim T, Bidone T, García-Aznar JM, Kamm RD (2012) Dynamic mechanisms of cell rigidity sensing: Insights from a computational model of actomyosin networks. *PLoS ONE* 7(11):e49174.
29. Zemel A, Rehfeldt F, Brown AEX, Discher DE, Safran SA (2010) Optimal matrix rigidity for stress fiber polarization in stem cells. *Nat Phys* 6(6):468–473.
30. Zemel A, Rehfeldt F, Brown AEX, Discher DE, Safran SA (2010) Cell shape, spreading symmetry and the polarization of stress-fibers in cells. *J Phys Condens Matter* 22(19):194110.
31. Curtis A, Aitchison G, Tsapikouni T (2006) Orthogonal (transverse) arrangements of actin in endothelia and fibroblasts. *J R Soc Interface* 3(11):753–756.
32. Trichet L, et al. (2012) Evidence of a large-scale mechanosensing mechanism for cellular adaptation to substrate stiffness. *Proc Natl Acad Sci USA* 109(18):6933–6938.
33. Marcq P, Yoshinaga N, Prost J (2011) Rigidity sensing explained by active matter theory. *Biophys J* 101(6):L33–L35.
34. Bischofs IB, Klein F, Lehnert D, Bastmeyer M, Schwarz US (2008) Filamentous network mechanics and active contractility determine cell and tissue shape. *Biophys J* 95(7):3488–3496.
35. Jiang H, Sun SX (2013) Cellular pressure and volume regulation and implications for cell mechanics. *Biophys J* 105(3):609–619.

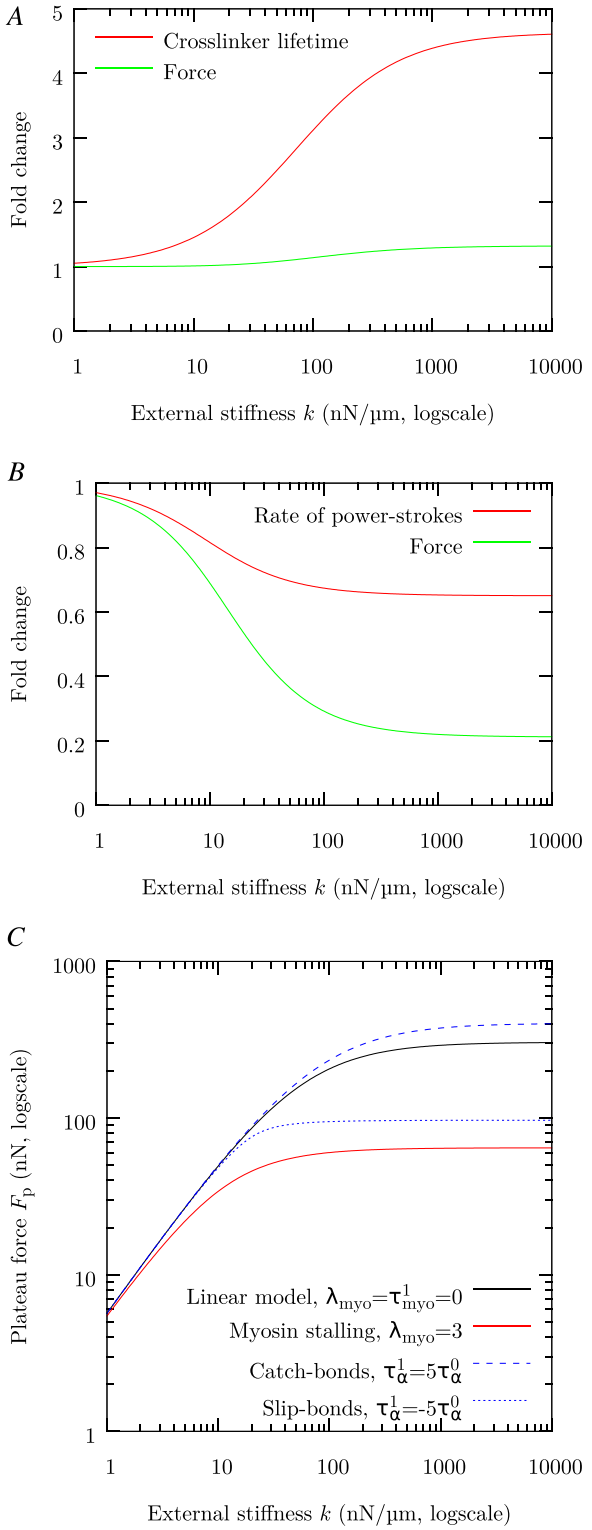

Fig. S1. Nonlinear extensions of the model. (*A*) Effect of catch bond-type cross-linkers. Taking $\tau_\alpha=\tau^0_\alpha+\tau^1_\alpha\sigma/E$ with $\tau^1_\alpha=5\tau^0_\alpha$ (*SI Text*, *S3.9*), a fivefold increase of cross-linker affinity under high external stiffness conditions is obtained, resulting in a 30% increase of the maximum force. (*B*) Effect of myosin stalling. Taking $\lambda_{myo}=3$ (*SI Text*, *S3.9*), a 30% decrease of the rate of myosin power strokes under high external stiffness conditions is obtained, resulting in a fivefold reduction of the plateau force. (*C*) Comparison of the model predictions of stiffness-dependent force in the cases of myosin stalling, catch bonds, and slip bonds. The mechanosensitivity caused by collective effects, with the minimal model that is the linear model, is preserved in the nonlinear cases.

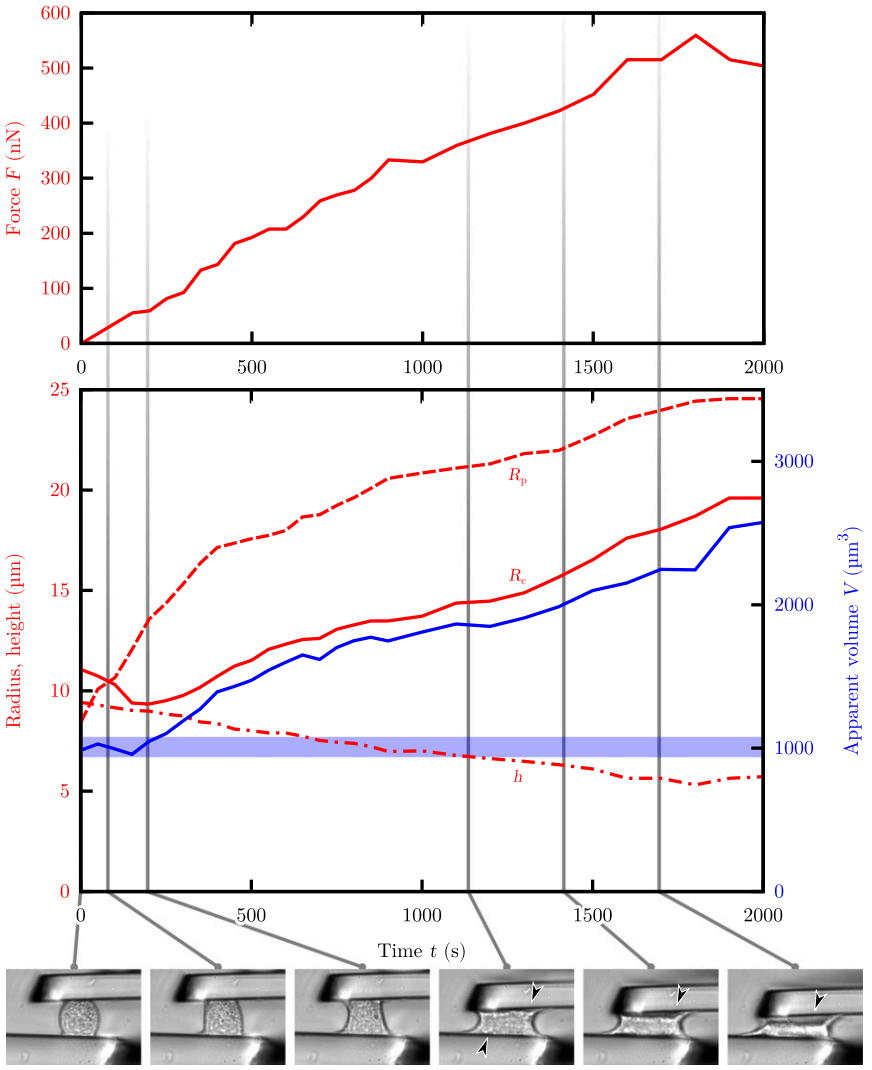

Fig. S2. Time evolution of the force and geometry of a single cell spreading between microplates of intermediate stiffness $k = 176$ nN/μm. (*Top*) The force grows until it reaches a maximum value. (*Middle*) Concurrently with the force increase, the cell spreads on the microplates, and R_p increases. The radius at the equator R_c also increases after a transient decrease. Both stabilize when the force is maximal. As the cell deflects the microplates, its half-length l decreases; however, this decrease does not compensate for the spreading in terms of (apparent) volume, and the volume V enclosed by the lateral cell surfaces increases more than twofold. (*Bottom*) Transmission images show that this apparent volume increase happens concurrently with the formation of pockets (arrowheads) away from the peripheral cell adhesions (Fig. S3*B*), where the cell locally detaches from the microplate. Details are in *SI Text*, *S5.1*.

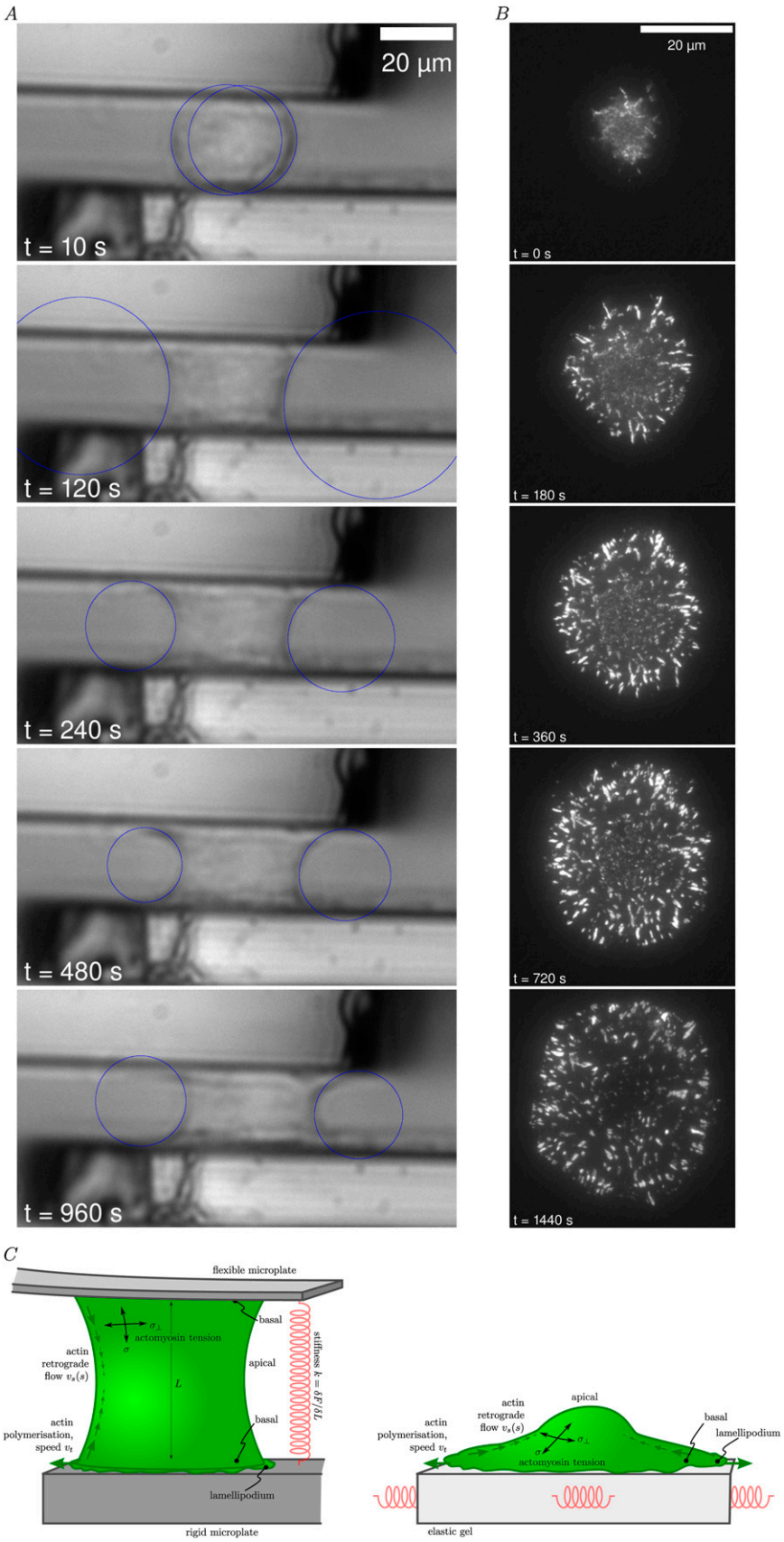

Fig. S3. (*A*) Light transmission image of a cell spreading on microplates with infinite stiffness *k* seen from the side. The sequence of shapes assumed by the cell walls in the course of an experiment can be described by arcs of circles. (*B*) TIRF visualization of fluorescent paxillin in a cell spreading on microplates with

Legend continued on following page

infinite stiffness k seen from the bottom. The spreading is isotropic, which supports the axial symmetry hypothesis. Adhesion zones are clearly apart from one another; along a circular region of interest, we find $N \simeq 40$ adhesion zones separated by paxillin-free passages of average width 1.5 μm (*SI Text*, *S5.1*). (*C*) Comparison of the features of cells spreading on (*Left*) two plates and (*Right*) a flat substrate. The spreading structure is preserved, with a lamellipodium structure at the front and more proximally, focal adhesions of increasing maturity as well as the different phases of spreading, rates of spreading, and focal adhesion dynamics (1). In cells spread on a flat substrate, actin polymerization at the edge and its retrograde flow compete to define the cell edge position and hence, the cell size (2). This regulation of cell size through a competition between polymerization and retrograde flow is also predicted by our model in the parallel plates geometry.

1. Fouchard J, et al. (2014) Three-dimensional cell body shape dictates the onset of traction force generation and growth of focal adhesions. *Proc Natl Acad Sci USA* 111(36):13075–13080.
2. Rossier OM, et al. (2010) Force generated by actomyosin contraction builds bridges between adhesive contacts. *EMBO J* 29(6):1055–1068.

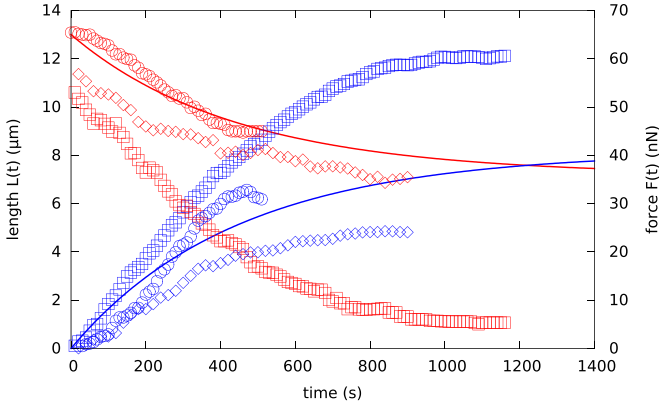

Fig. S4. Comparison of the model prediction of dynamics of cell contraction with experimental observations of individual cells. Symbols measured force (blue) and length (red) for three different cells contracting against a fixed external stiffness $k = 7$ nN/μm. These three cells are seen to have a different size (initial length ∼10.5, ∼11.5, and ∼13 μm) and different but comparable dynamics. Solid lines show 1D model predictions (without any fitting) using actomyosin parameters σ_a, E, τ_α, and v_t determined independently of the $k = 7$ nN/μm data and are valid for experiments over the whole range of external stiffness (Fig. 2).

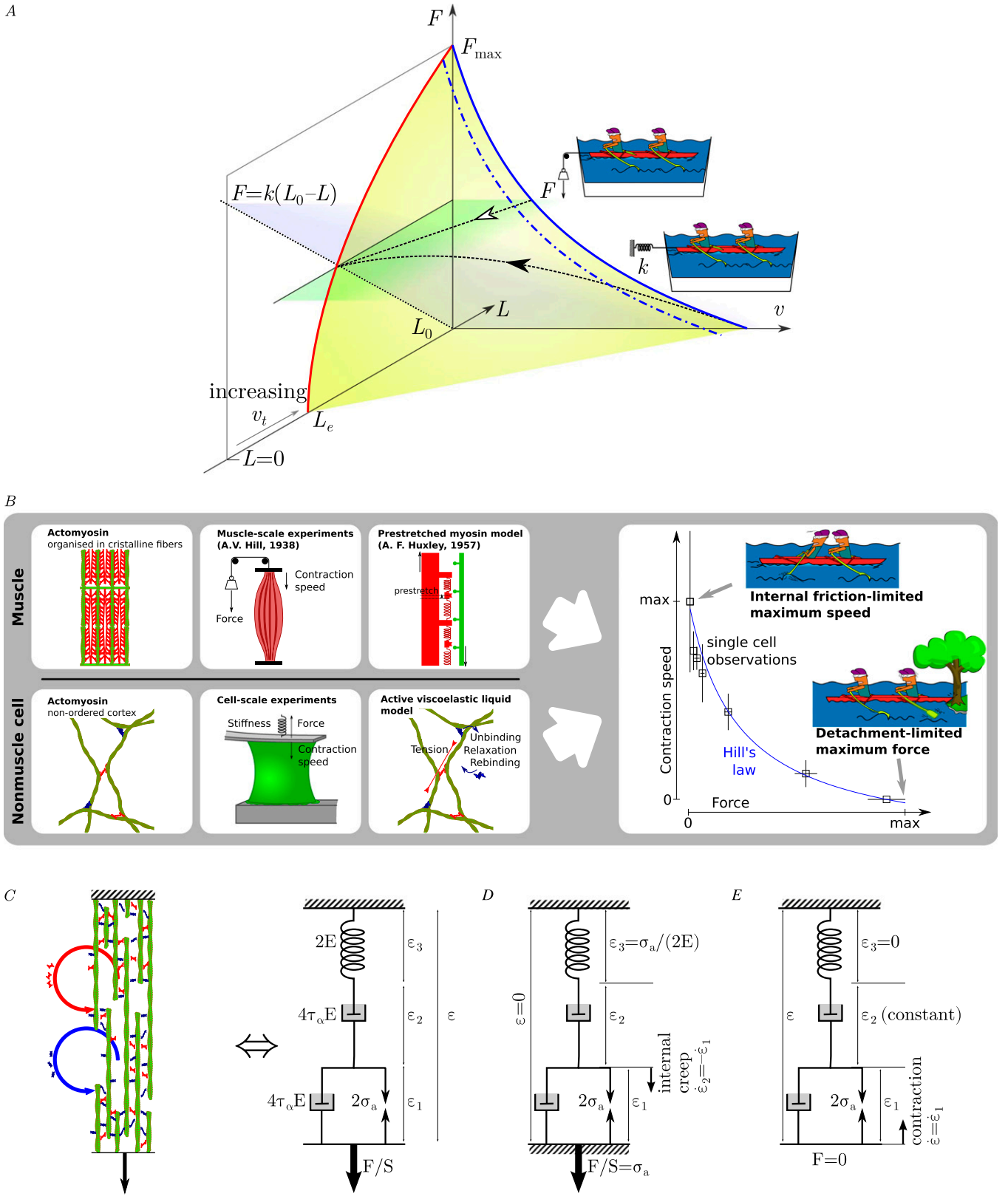

Fig. S5. (*A*) Sketch of the phase portrait of active contraction against a load or a spring. Muscle contraction experiments performed by Hill (1) correspond to contraction under a fixed load *F* (open arrowhead). The so-called Hill curve links this imposed force and the initial speed of retraction (solid blue curve). This model predicts a similar curve for cell contraction and the following dynamics, corresponding to decreasing length *L* until an equilibrium length L_p is reached as the contraction speed *v* vanishes. This length L_p is force-dependent (red curve). If treadmilling was absent, the limit of this curve would be a force-independent final length for any $F < F_{max}$ and a length-independent force F_{max} necessary to maintain any positive length. Experiments with cells cannot be performed at constant force as in the case of muscles, because cells need to adhere and spread (2). These experiments are performed here at constant stiffness *k*; thus, the

Legend continued on following page

trajectory in the phase portrait is in a plane defined by $F = k(L_0 - L)$ (solid arrowhead). The curve that we report in ref. 2 and compare with Hill's curve needs, thus, to be acquired for some fixed small deflection $\delta = 1\mu m$ (dot dash blue line), for which tuning k allows us to obtain any level of force $F = k\delta$. (*B*) The limiting factors setting a maximum speed and force are of the same nature in both the case of muscle contraction (3) and this model. As illustrated in these cartoons, the maximum speed arises when there is no external force, but the speed is such that some of the rowers generate friction before lifting up their oars and thus, counteract, in part, the pushing of the others (i.e., myosins do not have time to detach). The maximum force, at zero speed, arises from the fact that myosins detach after their stroke (as rowers will lift their oars) and thus, lose the elastic energy that they had achieved in the stroke, bending their oar. (*C*) A schematic of the rheological model (Eq. **2**) of actomyosin. The schematic using a spring of stiffness E, two dashpots of viscosity $2\tau_\alpha E$, and a perfect generator of tension σ_a illustrates the function of the rheological model in the cases $k = \infty$ and $k = 0$ but has no molecular-scale relevance. (*D*) For $k = \infty$, the total deformation ε has to be zero. At steady state, the tension is constant, and thus, $\varepsilon_3 = F/(SE)$ is constant as well: hence, $\varepsilon_2 + \varepsilon_1$ is also constant. The tension $2\sigma_a$, thus, elicits equal and opposite tensions σ_a in both dashpots, contracting one $[\dot{\varepsilon}_3 = -\sigma_a/(\tau_\alpha E)]$ and extending the other $[\dot{\varepsilon}_2 = \sigma_a/(\tau_\alpha E)]$, which illustrates the internal creep. (*E*) For $k = 0$, the tension in the main branch is zero, and thus, the spring and dashpot ε_2 do not work. Thus, tension $2\sigma_a$ is entirely absorbed by the dashpot ε_3, which contracts in doing so; thus, $\dot{\varepsilon} = \dot{\varepsilon}_3 = -\sigma_a/(\tau_\alpha E)$ until the system reaches an equilibrium length (*SI Text*, *S3.2* shows the additional role of treadmilling in this process, which is not shown here).

1. Hill AV (1938) The heat of shortening and the dynamic constants of muscle. *Proc R Soc Lond B Biol Sci* 126(843):136–195.
2. Mitrossilis D, et al. (2009) Single-cell response to stiffness exhibits muscle-like behavior. *Proc Natl Acad Sci USA* 106(43):18243–18248.
3. Huxley AF (1957) Muscle structure and theories of contraction. *Prog Biophys Biophys Chem* 7:255–318.

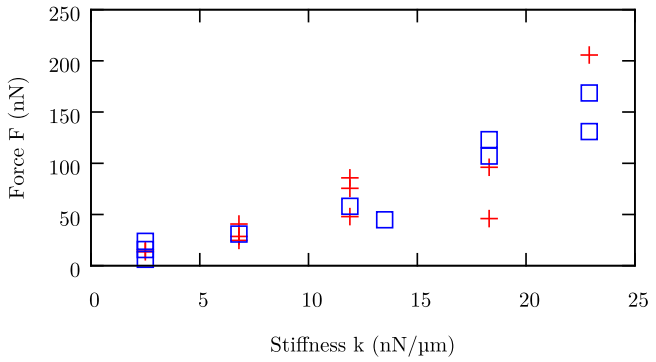

Fig. S6. Microtubules have a negligible influence on stiffness-dependent force generation. Blue boxes show plateau forces exerted by cells in microplate experiments in the presence of 1 μM Colchicine. Red crosses show controls. Discussion is in *SI Text*, *S1*.

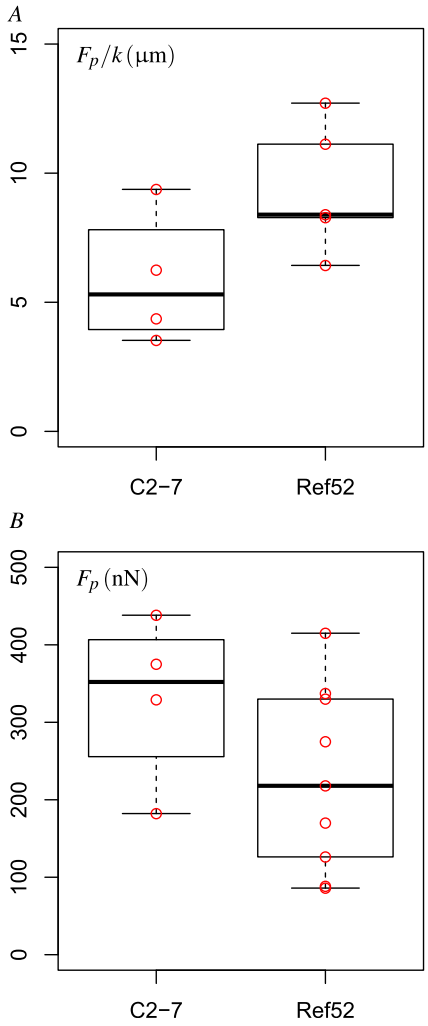

Fig. S7. Plateau force measured for two different cell types: Ref52 fibroblasts and C2-7 myoblasts. (*A*) Plateau force divided by external stiffness F_p/k micrometers for $k < k_c$. Welch two-sample *t* test cannot discriminate them (*P* value $0.083 > 0.05$). (*B*) Plateau force F_p for $k > k_c$ in nanonewtons. Welch two-sample *t* test cannot discriminate them (*P* value $0.17 > 0.05$).